A Simple Optical Fiber SPR Sensor With Ultra-High Sensitivity for Dual-Parameter Measurement

Farhan Mumtaz, Muhammad Roman, Bohong Zhang, *Graduate Student Member, IEEE*, Lashari Ghulam Abbas, Muhammad Aqueel Ashraf, Muhammad Arshad Fiaz, Yutang Dai, and Jie Huang, *Senior Member, IEEE*

***Abstract*—This work reports a simple optical fiber Surface Plasmon Resonance (SPR) sensor with ultra-high sensitivity for simultaneous measurement of the dual-parameter. The sensor is based on a D-shaped fiber with a nanolayer coating of Silver (Ag) and Hematite ($\alpha-Fe_2O_3$). The Ag/$\alpha-Fe_2O_3$ layer is deposited on the longitudinal surface of residual cladding, and a Fiber Bragg Grating (FBG) is inscribed on the single-mode fiber (SMF) for temperature compensation. The $\alpha-Fe_2O_3$ layer protects the Ag layer from oxidation and effectively enhances the surface plasmon wave while interacting with free electrons. Finite Element Method (FEM) modeling is employed to investigate the refractive index (RI) and temperature response of the SPR sensor. The SPR sensor exhibits an ultra-high RI sensitivity of 8,518 nm/RIU (refractive index unit) in the RI range of 1.33 to 1.40, and a temperature sensitivity of −52 pm/°C in the temperature range of 20 °C to 60 °C. The SPR performance suggests that it is a potential candidate for various applications of dual-parameter sensing.**

***Index Terms*—SPR sensor, D-shaped fiber, FBG, hematite, silver coating.**

I. Introduction

SPR devices are gaining popularity due to their capabilities of high sensitivity, rapid measurement speed, compactness, and reliability. Over the decades, many SPR sensor configurations [1] have been reported, and a range of biosensors and chemical sensors have been demonstrated for commercial purposes. SPR biosensors study the interaction among biomolecular substances, which is an essential aspect for biosensing. SPRs have been used in various fields, such as chemical/ biological analyte sensing, medical diagnostics, and environmental monitoring. When a surface plasmon wave is excited, a transverse magnetic polarized light is generated and interacts with the metal-dielectric interface to trigger charge density oscillations The SPR determines the expected RI variation from the resonance angle and wavelength. A thin layer of Ag typically exhibits better detection accuracy (DA) and sensitivity than Gold (Au) because Ag coating has a higher ratio of real and imaginary permittivity and higher reflection and absorption coefficients. The higher sensitivity of the SPR sensor depends on the relationship between excitation frequency ω and absorption frequency ω_0 of the metal layer [2]. For example, when $\omega < \omega_0$, the SPR sensor exhibits higher sensitivity than the case when $\omega \geq \omega_0$. Brujin et al. [3] also reported the choice for the metal layer in their SPR to achieve the best sensitivity results and showed that Ag offers better RI sensitivity than other metals.

SPR sensors have been widely reported for RI sensing only [4], [5], [6], [7], [8], [9], with the dual-parameter sensing aspect being neglected. One reason is that a single resonance SPR sensor is unreliable for dual-parameter measurement due to the temperature-RI crosstalk. In practical applications, dual-parameter measurement capability is highly advantageous due to ambient disturbances in temperature, humidity, and pressure. RI and temperature are the most common dual parameters for SPR sensing applications. Temperature-RI crosstalk must be addressed for practical applications. To solve the issue, several techniques have been employed to implement reliable SPR sensors. Several SPR sensor designs have been reported for RI detection with temperature compensation, such as hybrid SPR [10], multi-channel SPR [11], photonic crystal fiber (PCF) based SPR [12], polymer-coated side-polished SPR [13], nanolayers/wires based SPR [14], etc. Hybrid SPR [10] is the use of a SPR sensor in combination with another fiber optic sensor such as Mach-Zehnder interferometer and Fabry-Perot interferometer. Such structures can be implemented in a single optical fiber for ease of interrogation. Channel SPR [11] is designed by adding a sensing 'channel' in close proximity to the SPR sensor that enhances the dual-parameter measurement. PCF-based SPR [12] is capable of generating multiple SPR regions due to the multi-air hole design of the PCF, but it is a considerably expensive device. Polymer-coated SPR [13] has a hetero-core fiber structure that can also be used for dual-parameter measurement. However, due to the multimodal interference, the SPR spectrum is typically challenging to track, and thus additional signal processing is needed. Nanolayers/wires based SPR [14] were recently reported to increase the measurement sensitivity with complex structure designs.

Manuscript received 28 August 2022; accepted 31 August 2022. Date of publication 5 September 2022; date of current version 23 September 2022. *(Corresponding authors: Farhan Mumtaz; Jie Huang.)*

Farhan Mumtaz, Muhammad Roman, Bohong Zhang, and Jie Huang are with the Department of Electrical and Computer Engineering, Missouri University of Science and Technology, Rolla, MO 65409-0040 USA (e-mail: mfmawan@mst.edu; mroman@mst.edu; bzdtx@umsystem.edu; jieh@mst.edu).

Lashari Ghulam Abbas is with the Electrical Engineering Department, Sukkur IBA University, Sukkur, Sindh 65200, Pakistan (e-mail: ghulamscut@gmail.com).

Muhammad Aqueel Ashraf and Muhammad Arshad Fiaz are with the Communications Laboratory, Department of Electronics, Quaid-i-Azam University, Islamabad 45320, Pakistan (e-mail: aqueel@qau.edu.pk; arshadfiaz@qau.edu.pk).

Yutang Dai is with the National Engineering Laboratory for Fiber Optic Sensing Technology, Wuhan University of Technology, Wuhan 430070, China (e-mail: daiyt6688@whut.edu.cn).

Digital Object Identifier 10.1109/JPHOT.2022.3203930

This work is licensed under a Creative Commons Attribution 4.0 License. For more information, see https://creativecommons.org/licenses/by/4.0/

To increase the measurement sensitivity in refractive index for SPR sensors, several D-shaped SPR sensors have been reported with Ag and Au coatings [15], [16]. D-shaped SPR sensor with a coating of Graphene oxide and Ag exhibited a RI sensitivity of 833 nm/RIU [15]. Another D-shaped SPR sensor based on Au-grating structure demonstrated a RI sensitivity of 3340 nm/RIU [16]. The use of Graphene with a metal oxide layer on D-shaped SPR sensor improved the RI sensitivity to 5700 nm/RIU [17]. Also, a D-shaped structure with a grating of Ag/ Au$-\alpha-Fe_2O_3$ reported a maximum RI sensitivity of 6400 nm/RIU [18]. The inscription of the grating structure is quite complex and requires a stringent fabrication process. With the addition of the iron-oxides, the effective absorption coefficient is increased so that the sensitivity of the SPR sensor is enhanced correspondingly. In addition, these iron oxides are abundant, non-toxic, have a high corrosion resistance, air stability and are cost-effective, making them good candidates for better SPR sensor inventions. Several iron-oxides [19] are formed by Germanium, which includes $\alpha-Fe_2O_3$, maghemite ($\gamma-$ Fe_2O_3), magnetite (Fe_3O_4), and others. To protect the Ag layer from oxidation, the iron oxide film can easily be sputtered on the Ag layer via magnetron sputtering.

In this study, a highly sensitive D-shaped SPR sensor with a Ag/$\alpha-Fe_2O_3$ layered structure is investigated for dual-parameter measurement via FEM simulations. The sensitivity and DA of the SPR are tuned by optimizing the thickness of the Ag (T_{Ag}) and $\alpha-Fe_2O_3$ layers ($T_{Fe_2O_3}$) and residual cladding (D_{res}). The RI measurement sensitivity is drastically improved through parametric optimization. A cascaded FBG is included for temperature compensation along with analyte detection. At the time of this writing, the reported SPR sensor exhibits the highest sensitivity in RI (e.g., 8518 nm/RIU) among the reported optical fiber-based SPR sensors for dual-parameter measurement. Another advantage of the reported SPR sensor is the simplicity of the SPR structure in comparison with the grating-based Ag/ Au$-\alpha-Fe_2O_3$ SPR sensor.

This paper is organized as follows: Section II presents SPR structural design and working principle. Section III provides the results and discussion, and Section IV illustrates the research conclusions.

II. Sensor Design and Principle

The schematic diagram of the proposed SPR sensor is shown in Fig. 1(a), and its longitudinal cross-section cascaded with FBG structure can be seen in Fig. 1(b). The core and cladding diameters of the D-shape fiber are 8.2 μm and 125 μm, respectively, while D_{res} is taken as 100 nm. The Sellmeier equation is used to define the wavelength-dependent RI of the core (GeO_2-doped silica) and cladding (Pure silica) by [18],

$$n(\lambda) = \sqrt{1 + \frac{a_1\lambda^2}{\lambda^2 - b_1^2} + \frac{a_2\lambda^2}{\lambda^2 - b_2^2} + \frac{a_3\lambda^2}{\lambda^2 - b_3^2}} \quad (1)$$

where *a* and *b* are the Sellmeier coefficients for core and cladding of the D-shaped fiber, and their values are listed in Table I. In geometry, $T_{Fe_2O_3}$ and T_{Ag} depict the thickness of the Ag and $\alpha-Fe_2O_3$ layers, respectively, and *W* represents the width of

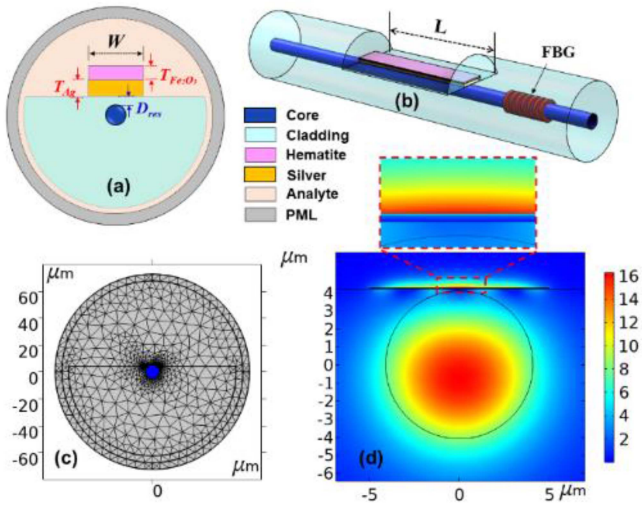

Fig. 1. Schematic diagram of proposed SPR sensor and its (a) Transverse cross-section, (b) Longitudinal cross-section, (c) Mesh by COMSOL, and (d) SPR Electric field mode at the $\lambda_0 = 1.044$ μm.

TABLE I
Important Coefficients

Description	Term and Values
Sellmeier coefficients of core and cladding	*GeO_2-doped silica:* $a_1 = 0.702854$; $a_2 = 0.4146307$; $a_3 = 0.8974540$; $b_1 = 0.0727723$; $b_2 = 0.1143085$; $b_3 = 9.896161$
	Pure silica: $a_1 = 0.6961663$; $a_2 = 0.4079426$; $a_3 = 0.8974794$; $b_1 = 0.0684043$; $b_2 = 0.1162414$; $b_3 = 9.896161$
Dispersion coefficients of Ag	$\lambda_c = 17.614$
	$\lambda_p = 0.14541$

both layers. FBG is inscribed at a Bragg wavelength of 632 nm for temperature compensation.

Assume a p-polarized incident light whose tangential field components are continuous across the interface, and its complex wavevector "k_x" determines the surface plasmon wavevector either by incidence angle or light wavelength. Sharma et al. [20] explored the dielectric equation and dependencies of surface plasmon wavevector, which deduces the dispersion relationship for a given geometry as,

$$k_{spw} = \frac{2\pi}{\lambda_0}\sqrt{\frac{n_{Ag}^2 n_{\alpha-Fe_2O_3}^2 \mathrm{RI}_{ext}^2}{n_{Ag}^2 + n_{\alpha-Fe_2O_3}^2 + \mathrm{RI}_{ext}}} \quad (2)$$

where λ_0 represents the operating wavelength of the light source, *n* denotes the refractive index, and the sub-scripts are self-explanatory for materials. A matching condition met when there is continuity between the longitudinal component of the light propagation constant and surface plasmon oscillations at the interface of dielectric and metallic layers. Permittivity of the Ag layer is derived by using the Drude dispersion model [4], which is used to determine the wavelength-dependent dielectric

constant of the metal layer as,

$$\varepsilon_{Ag}(\lambda) = 1 - \frac{\lambda^2 \lambda_c}{\lambda_p^2 (\lambda_c + i\lambda)} \tag{3}$$

where λ_c and λ_p are the wavelengths related to collision losses and bulk plasma frequency, respectively, and their values are given in Table I. Querry [21] reported a wavelength-dependent RI model to estimate the RI of $\alpha-Fe_2O_3$. $\alpha-Fe_2O_3$ carries high absorption features, and is capable of preventing metal from oxidation, i.e., $\alpha-Fe_2O_3$ coating on Ag film eliminates the risk of metal oxidation. For the proposed SPR sensor, the employment of a $\alpha-Fe_2O_3$ coating on the Ag layer prevents the tendency of oxidation. Additionally, the $\alpha-Fe_2O_3$ layer enhances the extinction ratio of SPR-dip. In contrast, the SPR sensors with a single Ag layer are unable to produce SPR-dip with a large extinction ratio. Further, SPR-dip also depends on the phase-matching condition between surface plasmon mode and fundamental mode. When the phase-matching condition is satisfied, it can be expressed as [22],

$$n_{co} \sin \theta_c = \sqrt{\frac{\varepsilon_{ext}\varepsilon_{Ag}}{\varepsilon_{ext} + \varepsilon_{Ag}}} \tag{4}$$

where ε_{ext} is the dielectric constant of the external medium, θ_c is the critical angle of the incident light, and n_{co} denotes the refractive index of the core.

The total transmitted power depends on the transmission function and normalized source power of p-polarized light, which can be estimated by [18],

$$T = \exp\left(\frac{-4\pi}{\lambda_0} \text{imag}\left(n_{eff}\left(\lambda, \text{RI}_s, T_s\right)\right) \times L\right) \tag{5}$$

where, $n_{eff}(\lambda, \text{RI}_s, T_s)$ refers to the effective refractive index of the fundamental mode of optical fiber, and L is the sensing length which is taken as 1 mm. RI_s and T_s represent surrounding RI and temperature, respectively. Cascaded with the SPR sensor, an FBG is inscribed on a SMF, which is periodically demodulated along the core axis of the fiber. It reflects the intensity of light at a specific wavelength and transmits the rest of the light. Thus, the Bragg wavelength of FBG can be estimated as [23],

$$\lambda_{\text{FBG}} = 2n_{eff}^{co}\left(\lambda, T_s\right) \times \Lambda\left(T_s\right) \tag{6}$$

where Δn_{eff}^{co} (λ, T_s) refers to the effective index of the core mode and $\Lambda(T_s)$ denotes periodic RI modulations. Both are sensitive to T_s change. SPR sensor performance exclusively depends on RI sensitivity (S_{RI}) and DA, which is fundamentally affected by the change in wavelength and effective RI. S_{RI} refers to the wavelength interrogation method and can be estimated as [12],

$$S_{\text{RI}} = \frac{\Delta\lambda_0}{\Delta n_{eff}} \tag{7}$$

And temperature sensitivity S_T of the given sensor can be estimated as,

$$S_T = \frac{\Delta\lambda_0}{\Delta T} \tag{8}$$

The performance of the SPR sensor is mainly dependent on S_{RI} and DA of the SPR-sensor. Whereas DA is inversely proportional to the full width at half maximum (FWHM), and can be defined as [24],

$$\text{DA} = \frac{1}{\text{FWHM}} \tag{9}$$

FWHM is measured in *nm* and is calculated at the resonant dip of SPR sensor in the transmission spectrum by (5). The figure of merit (FOM) for the proposed SPR sensor is measured as,

$$\text{FOM} = \frac{S_\lambda}{\text{FWHM}} \tag{10}$$

S_λ is derived from (7) and FOM is measured in RIU^{-1}.

III. Result & Discussion

A. Input Parameters

Wave optic module of COMSOL Multiphysics 5.6 is used to determine variations in RI_s and T_s. Fig. 1(a) shows the geometry of the SPR sensor and is built using the following parameters. The main components of the SPR sensor geometry consist of core, cladding, Ag layer, $\alpha-Fe_2O_3$ layer, analyte, and a perfect match layer (PML), where PML defines the boundary conditions for the precise modal solutions. A built-in function of extremely fine meshing of elements is chosen to define SPR boundaries, domains, and points. The meshing statistics are defined as follows: the total vertices = 4; total domain elements = 240; total boundary elements = 32; total elements = 19602; minimum element quality = 0.1358 and average element quality = 0.6591; and mesh of the SPR sensor is sketched in Fig. 1(c). The electric field mode for SPR sensor is obtained by using FEM with $T_{Fe2O3} = 12$ nm, $T_{Ag} = 50$ nm, $W = 10$ μm, $D_{res} = 100$ nm and $\text{RI}_s = 1.39$. Equation (1) is used to calculate the RIs of the core and cladding for SPR. Equation (2) describes the occurrence of the SPR phenomenon when incident wavevector and plasmon wavevector are harmonized with each other. The energy carried by the core will be transferred to the sensing region via the Ag/$\alpha-Fe_2O_3$ layer. Consequently, the strength of the evanescent field is enhanced due to the higher absorption coefficient of $\alpha-Fe_2O_3$, as shown in Fig. 1(d). Whereas a higher absorption coefficient of the metallic layer in SPR configurations improve the strength of the evanescent field and ensures higher sensitivity [2]. Equation (3) derives the permittivity of Ag and (4) derives the transmission function of the SPR sensor. A wavelength range of 0.6 μm to 1.3 μm is used to calculate the transmission spectrum with a wavelength step size of 0.01 nm. D_{res} of 100 nm is used to withstand the conjunction between surface plasmon mode and fundamental mode.

B. Sensor Optimization

The SPR is optimized by evaluating a few key parameters: T_{Ag} of 50 nm is fixed. T_{Fe2O3} is swept from 4 nm to 16 nm to examine the influence of dip visibility and stability. As shown in Fig. 2(a), the SPR-dip exhibits a non-symmetric feature. The right side of the resonant dip (i.e., rising curve) shows a higher attenuation in comparison with the left side (i.e., falling curve). As T_{Fe2O3} increases from 4nm to 16 nm, the strength of the

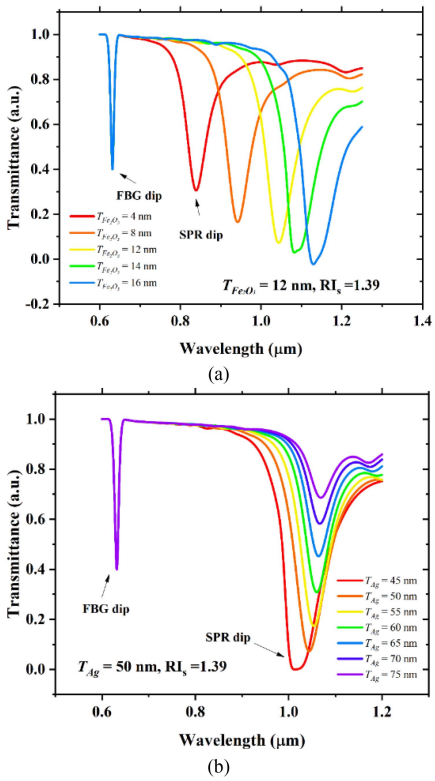

Fig. 2. SPR sensor and FBG interference spectrum; when (a) $T_{Ag} = 50$ nm and T_{Fe2O3} is varied from 4 - 16 nm, and (b) $T_{Fe2O3} = 12$ nm and T_{Ag} is varied from 45 - 70 nm.

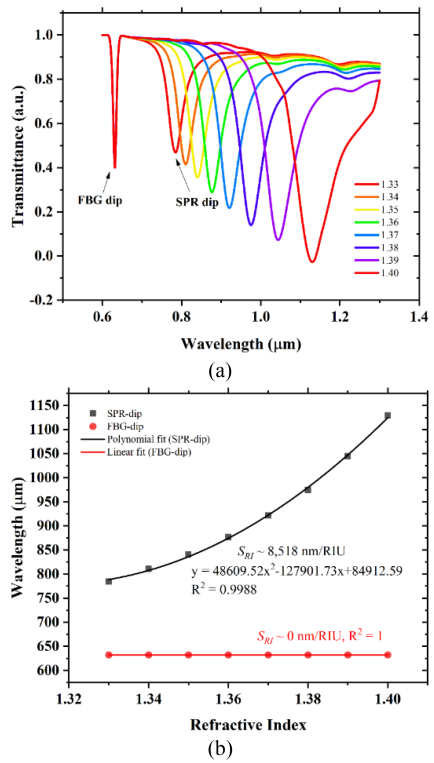

Fig. 3. (a) RI measurements response of proposed SPR sensor, (b) S_{RI} of SPR and FBG at different values of analytes.

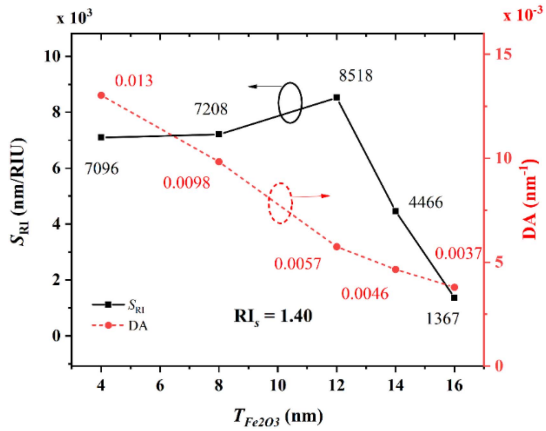

Fig. 4. S_{RI} and DA variations with different T_{Fe2O3} layers.

SPR-dip increases correspondingly. However, the transmission attenuation of the right side of the SPR-dip also increases for higher T_{Fe2O3}, and the resonant dips are distorted Considering the high resonant strength, low attenuation, and zero distortion, T_{Fe2O3} of 12 nm is chosen. Similarly, T_{Fe2O3} of 12 nm is fixed, and then T_{Ag} is swept from 45 nm to 75 nm. The increase of T_{Ag} weakens the SPR-dip intensity. From Fig. 2(b), a secondary SPR-dip is introduced by the SPR sensor when T_{Ag} reaches 60 nm, which is due to the excitation of cladding modes. T_{Ag} of 50 nm offers the best extinction ratio and visibility of SPR-dip. FBG interference dip is derived by (6). Fig. 2(a) and (b) illustrate that the FBG-dip remains at 632 nm at various SPR excitation conditions, indicating that the Bragg wavelength is neither affected by SPR nor RI$_s$. Fig. 2(a), it can be seen when the SPR dip wavelength moved towards a longer wavelength, then SPR spectral dip further deepened with the increased T_{Fe2O3}. $W = 10\ \mu$m is adjusted. However, it does not reflect any change in the spectrum when it varies from 125 μm to 10 μm across the D_{res} surface. Although, when it is chosen less than 10 μm, it reduces the DA and shows a secondary SPR-dip which deteriorates the light strength and does not help to radiate a stronger evanescent field. During several iterations, the RI$_s$ value is set at 1.39.

C. RI Measurement Response

SPR sensor is also simulated to determine RI in the range of 1.33 to 1.40 at 20 °C. When RI$_s$ varies from 1.33 to 1.40, the SPR dip exhibits a red-shift and moves from 784.27 nm to 1129.55 nm, respectively, as shown in Fig. 3(a). Whereas the FBG-dip remains constant at the wavelength of 632 nm, as FBG is not affected by the RI$_s$. Changes caused by the localization of guided modes in the SMF, which indicates that FBG is insensitive to RI$_s$. The optimization of the SPR sensor has significantly enhanced the S_{RI} up to 8518 nm/RIU at the RI range of 1.39 to 1.40 and showed a DA of 0.006 nm^{-1}. SPR-dip exhibits a maximum ultra-high S_{RI} of 8518 nm/RIU with an excellent polynomial fitting of 0.9988, and as expected, the FBG-dip exhibits S_{RI} of 0 nm/RI, as shown in Fig. 3(b). Fig. 4 depicts that the SPR sensor's S_{RI} increases from 7096 nm/RIU to 8518 nm/RIU when T_{Fe2O3}

TABLE II
PARAMETERS OF PROPOSED SPR SENSOR

RI	Dip position (nm)	SPR-dip shift (nm)	S_{RI} (nm/RIU)	Measurement Resolution (RIU)	FWHM (nm)	DA (nm^{-1})	FOM (RIU^{-1})
1.33	784.27	26.00	2600	3.84×10^{-6}	39.39	0.025	66.01
1.34	810.62	26.35	2635	3.79×10^{-6}	44.00	0.023	59.89
1.35	840.15	29.53	2953	3.38×10^{-6}	49.90	0.020	59.18
1.36	876.82	36.67	3667	2.72×10^{-6}	56.20	0.018	65.25
1.37	921.27	44.45	4445	2.24×10^{-6}	64.74	0.015	68.66
1.38	974.73	53.46	5346	1.87×10^{-6}	76.89	0.013	69.53
1.39	1044.37	69.64	6964	1.43×10^{-6}	97.90	0.010	71.13
1.40	1129.55	85.18	8518	1.17×10^{-6}	161.70	0.006	52.68

increases from 4 to12 nm with a constant T_{Ag} of 50 nm. When T_{Fe2O3} increases through the range of 12 nm to 16 nm, the S_{RI} drops substantially to 1367 nm/RIU at RI_s of 1.40. Interestingly, there is turning point around 12 nm, typically called critical coupling point. The regions at T_{Fe2O3} greater and less than 12 nm are over-coupled and under-coupled, respectively. S_{RI} depends on the absorption coefficient of the $\alpha-Fe_2O_3$ layer and the critical coupling condition. Higher absorption coefficient of $\alpha-Fe_2O_3$ with the critical coupling state point can be obtained by reducing the T_{Fe2O3} to around 12 nm. The analysis helps to determine the highest S_{RI} with the most suitable T_{Fe2O3} and T_{Ag}.

On the contrary, the tendency of DA decreases from 0.025 to 0.006 nm^{-1} when T_{Fe2O3} increases from 4 to 16 nm. During the investigation, it was observed that the T_{Fe2O3} greatly influenced the S_{RI} as well as DA of the proposed SPR sensor. The minimum and maximum FOM varies from 52.1 to 77.13 RIU^{-1}. The essential parameters of the SPR sensor with measured values (i.e., S_{RI}, measurement resolution, FWHM, DA, FOM) are listed in Table II.

D. Temperature Measurement Response

When T_s varies from 20 °C to 60 °C, the effective refractive indices also vary due to the thermo-optic effect of the silica cladding and doped-silica core of the SPR sensor. The refractive index of the SPR sensor with respect to the change in T_s can be estimated as [25],

$$n_m\left(T_o + \Delta T\right) = n_m T_o + \xi_m \Delta T \tag{11}$$

where the subscript m represents the core and cladding mode, T_o is the initial temperature, ΔT is the temperature change, ξ is the thermo-optic coefficient ($\sim 4.1 \times 10^{-7}$/°C at room temperature [26]) with the assumption of the same values for core and cladding. Spectral evolution consists of comparing the SPR-dip to the FBG-dip. Both dips show responses to T_s which is due to a slight difference between the thermo-optic coefficient of core and cladding mode. SPR-dip produces a blue shift, whereas FBG-dip produces a red-shift in the transmission spectrum, which is consistent with the theory. The transmission spectra at various ambient temperatures are shown in Fig. 5(a). (6) estimates the FBG-dip movement with respect to the change in T_s. The optimum thickness of a $\alpha-Fe_2O_3$ layer of 12 nm combined with a Ag layer of 50 nm causes weak blueshifts of the longitudinal localized SPR mode when experiencing a change in temperature, while the same thickness of $\alpha-Fe_2O_3$ with Ag causes large redshifts when a change in RI_s is observed. The redshifts are possibly due to a reduced plasmon-coupling effect [27] with the excitonic region of $\alpha-Fe_2O_3$. The observed large redshifts in the SPR peak position are possibly due to surface modification between $\alpha-Fe_2O_3$ and Ag. From the insets of Fig. 5(a), the spectral evolutions of the SPR dips and FBG dips can both be observed with T_s change from 20 °C to 60 °C when RI_s is set at 1.39. The Blue inset represents a zoomed-in region of the FBG-dip evolution while the pink inset represents the SPR-dip evolution. From Fig. 5(b), the maximum temperature sensitivities of −52.1 pm/°C and 10 pm/°C with linear correlation fitting of 0.998 and 0.99 are achieved for the SPR sensor and the FBG, respectively. The two different temperature sensitivities can be used for temperature compensation.

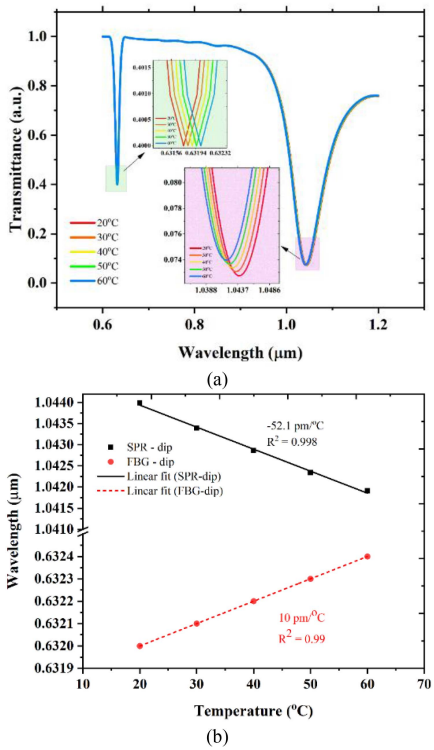

Fig. 5. (a) Temperature response of SPR sensor and FBG, (b) Temperature sensitivities with linear correlation function.

E. Simultaneous Measurement of Dual-Parameter

It can be inferred from RI and temperature measurements; the resonant dips produce different responses to RI_s and T_s.

TABLE III
SPR - COMPARISON

SPR sensors	S_{RI} (nm/RIU)	RI range	RI Measurement Resolution (RIU)	S_T (pm/°C)	T- Range	Structure
D-shaped (Graphene Oxide) [15]	833.33	(1.30-1.34)	1.20×10^{-5}	-	-	Simple
Hybrid SPR [10]	1433	(1.33-1.35)	6.98×10^{-6}	-	-	Simple
D-shaped (Au-grating) [16]	3340	(1.36-1.38)	2.99×10^{-6}	-	-	Complex
D-shaped (Metal oxide coated) [17]	5570	(1.34-1.345)	1.80×10^{-6}	-	-	Simple
D-shaped (Ag/α−Fe_2O_3 Gratings) [18]	6400	(1.33-1.39)	1.56×10^{-6}	-	-	Complex
D-shaped PCF liquid filled [12]	2275	(1.00-1.60)	4.40×10^{-6}	9,090	(15-50°C)	Complex
Polymer coated side polish [13]	5000	(1.32-1.40)	2.00×10^{-6}	-978	(25-100°C)	Simple
Our research	8518_{SPR} 0_{FBG}	(1.33-1.40)	1.14×10^{-6} -	-52.1_{SPR} 10_{FBG}	(20-60°C)	Simple

Thus, RI and temperature measurements can be segregated via a sensitivity matrix equation which is typically used for the measurement of two or more parameters simultaneously. The sensitivity matrix for SPR sensor with cascaded FBG can be estimated by [28],

$$\begin{bmatrix} \Delta \mathrm{RI} \\ \Delta T \end{bmatrix} = \begin{bmatrix} \sigma_{\mathrm{RI,SPR}} & \sigma_{T,\mathrm{SPR}} \\ \sigma_{\mathrm{RI,FBG}} & \sigma_{T,\mathrm{FBG}} \end{bmatrix}^{-1} \begin{bmatrix} \Delta\lambda_{\mathrm{SPR}} \\ \Delta\lambda_{\mathrm{FBG}} \end{bmatrix} \quad (12)$$

$$\begin{bmatrix} \Delta \mathrm{RI} \\ \Delta T \end{bmatrix} = \begin{bmatrix} 8518 & -52.10 \\ 0 & 10 \end{bmatrix}^{-1} \begin{bmatrix} \Delta\lambda_{\mathrm{SPR}} \\ \Delta\lambda_{\mathrm{FBG}} \end{bmatrix} \quad (13)$$

where $\sigma_{\mathrm{RI,SPR}}$, $\sigma_{\mathrm{RI,FBG}}$, $\sigma_{T,\mathrm{SPR}}$, and $\sigma_{T,\mathrm{FBG}}$ are sensitivity coefficients of RI and temperature for the SPR sensor and FBG, respectively. ΔRI and ΔT represent changes in RI and temperature, respectively. $\Delta\lambda_{\mathrm{SPR}}$ and $\Delta\lambda_{\mathrm{FBG}}$ represent changes in SPR-dip and FBG-dip, respectively. The measurement resolutions of 1.17×10^{-6} RIU and 1.9×10^{-1}°C for RI and temperature are obtained with a 0.01 nm tracing wavelength limit.

F. SPR Comparison and Potential Applications

It can be inferred from the results that the deposition of α−Fe_2O_3 on Ag in a layered SPR sensor can substantially enhance the sensitivity and generate an SPR dip with a large extinction ratio. The simple SPR sensor also has the advantage of ease of fabrication, user-reconfigurable, and mass production capability in comparison with the reported complex structures [12], [16], [18]. Table III lists various reported SPR sensors and compares the sensitivity, RI measurement range, measurement resolution, and method of fabrication. It can be summarized that the reported SPR sensor has a simple structure, dual-parameter sensing capability with a wide range of RI detection capability, and the highest measurement sensitivity. In addition, the reported sensor exhibits a high measurement resolution for RI.

SPR sensor cascaded with FBG offers a broader RI detection range, i.e., 1.33 to 1.40, and the temperature detection range is from 20 °C to 60 °C. The broad RI range covers a wide variety of chemical and biomedical analytes for dual-parameter detection. For example: It can use to examine chemical solutions such as, Alcohol (RI_s-1.33), methyl (RI_s-1.33), Ether (RI_s-1.35), acetone (RI_s-1.36), propylene (RI_s-1.36), ethanol (RI_s-1.361), hexane (RI_s-1.37), acetic acid (RI_s-1.37), trichlorofluoromethane (RI_s-1.37), heptane (RI_s-1.38), kerosene (RI_s-1.39), silicone oil (RI_s-1.393), and it is equally capable for testing of various diseases in the biomedical domain such as, plasma (RI_s-1.34), tuberculosis (RI_s-1.345 to 1.349), white blood cell (RI_s-1.36), skin cell (RI_s-1.36 to 1.38), cervical cell (RI_s-1.368 to 1.392), blood cells (RI_s-1.376 to 1.390), breast cancer cell (RI_s-1.385 to 1.401), etc.

IV. CONCLUSION

In summary, a simple optical fiber SPR sensor with ultra-high sensitivity is reported. SPR sensor consists of a segment of D-shaped fiber coating with Ag/α−Fe_2O_3. The dual-parameter analysis is carried out via FEM. T_{Ag}, T_{Fe2O3}, W, and D_{res} are major parameters of SPR which has been optimized in this study. The optimization of the SPR sensor dramatically influences the S_{RI}, DA, FOM, and measurement resolution. α−Fe_2O_3 plays a vital role in preventing the oxidation of Ag and generating a solid evanescent field in the sensing region with improved visibility of the resonant dip. A maximum S_{RI} of 8518 nm/RIU is achieved in the RI range of 1.33 to 1.40 with $R^2 = 0.9988$ using the polynomial fitting. The reported SPR sensor with dual-parameter measurement capability is a potential candidate for various chemical and biomedical applications.

DISCLOSURE

No potential conflict of interest is reported by Authors.

ACKNOWLEDGMENT

Jie Huang is grateful for support from the Roy A. Wilkens Professorship Endowment.

REFERENCES

[1] C. Chen and J. Wang, "Optical biosensors: An exhaustive and comprehensive review," *Analyst*, vol. 145, no. 5, pp. 1605–1628, 2020, doi: 10.1039/c9an01998g.

[2] B. D. Gupta and A. K. Sharma, "Sensitivity evaluation of a multi-layered surface plasmon resonance-based fiber optic sensor: A theoretical study," *Sensors Actuators, B Chem.,* vol. 107, no. 1, pp. 40–46, 2005, doi: 10.1016/j.snb.2004.08.030.

[3] H. E. De Bruijn, R. P. H. Kooyman, and J. Greve, "Choice of metal and wavelength for surface-plasmon resonance sensors : Some considerations," *Appl. Opt.*, vol. 31, no. 4, pp. 440–442, 1992.

[4] Y. Al-Qazwini, A. S. M. Noor, T. K. Yadav, M. H. Yaacob, S. W. Harun, and M. A. Mahdi, "Performance evaluation of a bilayer SPR-based fiber optic RI sensor with TiO_2 using FDTD solutions," *Photon. Sensors*, vol. 4, no. 4, pp. 289–294, 2014, doi: 10.1007/s13320-014-0207-y.

[5] N. Luan and J. Yao, "A hollow-core photonic crystal fiber-based SPR sensor with large detection range," *IEEE Photon. J.*, vol. 9, no. 3, Jun. 2017, Art no. 6802107, doi: 10.1109/JPHOT.2017.2694479.

[6] A. K. Mishra, S. K. Mishra, and B. D. Gupta, "SPR based fiber optic sensor for refractive index sensing with enhanced detection accuracy and figure of merit in visible region," *Opt. Commun.*, vol. 344, pp. 86–91, 2015, doi: 10.1016/j.optcom.2015.01.043.

[7] F. Wang, C. Liu, Z. Sun, T. Sun, B. Liu, and P. K. Chu, "A highly sensitive SPR sensors based on two parallel PCFs for low refractive index detection," *IEEE Photon. J.*, vol. 10, no. 4, Aug. 2018, Art no. 7104010, doi: 10.1109/JPHOT.2018.2856273.

[8] J. Wang, L. Pei, L. Wu, J. Wang, Z. Ruan, and J. Zheng, "A polarization-independent SPR sensor based on photonic crystal fiber for low RI detection," *Plasmonics*, vol. 15, no. 2, pp. 327–333, 2020, doi: 10.1007/s11468-019-01054-0.

[9] D. Yi et al., "Interrogation technique analyses of a hybrid fiber optic sensor based on SPR and MMI," *Opt. Exp.*, vol. 28, no. 14, pp. 20764–20772, 2020, doi: 10.1364/oe.396374.

[10] Z. Akbarpour, V. Ahmadi, and F. A. Roghabadi, "Enhanced Mach-Zehnder interferometer multimode–single-mode–multimode fiber optic refractive index sensor based on surface plasmon resonance," *Opt. Fiber Technol.*, vol. 73, 2022, Art. no. 103035, doi: 10.1016/j.yofte.2022.103035.

[11] P. Niu, J. Zhao, C. Zhang, H. Bai, and W. Shi, "Multi-channel optical fiber refractometer based on tree topology structure," *Appl. Opt.*, vol. 57, no. 16, pp. 4696–4700, 2018, doi: 10.1364/ao.57.004696.

[12] Y. Guo et al., "Amphibious sensor of temperature and refractive index based on D-shaped photonic crystal fibre filled with liquid crystal," *Liquid Cryst.*, vol. 47, no. 6, pp. 882–894, 2020, doi: 10.1080/02678292.2019.1686777.

[13] S. Liu, S. Cao, Z. Zhang, Y. Wang, C. Liao, and Y. Wang, "Temperature sensor based on side-polished fiber SPR device coated with polymer," *Sensors (Switzerland)*, vol. 19, no. 19, 2019, Art. no. 4063, doi: 10.3390/s19194063.

[14] N. Luan, R. Wang, W. Lv, Y. Lu, and J. Yao, "Surface plasmon resonance temperature sensor based on photonic crystal fibers randomly filled with silver nanowires," *Sensors (Switzerland)*, vol. 14, no. 9, pp. 16035–16045, 2014, doi: 10.3390/s140916035.

[15] I. S. Amiri et al., "Graphene oxide effect on improvement of silver surface plasmon resonance D-shaped optical fiber sensor," *J. Opt. Commun.*, 2019, doi: 10.1515/joc-2019-0094.

[16] J. L. U. Unjie, Y. L. I. An, Y. A. H. An, Y. I. L. Iu, and J. I. G. Ao, "D-shaped photonic crystal fiber plasmonic refractive index sensor based on gold grating," *Appl. Opt.*, vol. 57, no. 19, pp. 5268–5272, 2018.

[17] A. Patnaik, K. Senthilnathan, and R. Jha, "Graphene-based conducting metal oxide coated D-shaped optical fiber SPR sensor," *IEEE Photon. Technol. Lett.*, vol. 27, no. 23, pp. 2437–2440, Dec. 2015, doi: 10.1109/LPT.2015.2467189.

[18] R. A. Kadhim, L. Yuan, H. Xu, J. Wu, and Z. Wang, "Highly sensitive D-shaped optical fiber surface plasmon resonance refractive index sensor based on Ag-α-Fe_2O_3 grating," *IEEE Sens. J.*, vol. 20, no. 17, pp. 9816–9824, Sep. 2020, doi: 10.1109/JSEN.2020.2992854.

[19] L. R. Bernstein, "Germanium geochemistry and mineralogy," *Geochimica Cosmochimica Acta*, vol. 49, no. 11, pp. 2409–2422, 1985, doi: 10.1016/0016-7037(85)90241-8.

[20] A. K. Sharma, R. Jha, and B. D. Gupta, "Fiber-optic sensors based on surface plasmon resonance: A comprehensive review," *IEEE Sens. J.*, vol. 7, no. 8, pp. 1118–1129, Aug. 2007, doi: 10.1109/JSEN.2007.897946.

[21] M. R. Query, *Optical Constants of Minerals and Other Materials From the Millimeter to the Ultraviolet*. Chemical Research, Development & Engineering Center, US Army Armament Munitions Chemical Command, 1987.

[22] Y. Yu, P. Blake, and D. K. Roper, "Tapered optical fibers designed for surface plasmon resonance phase matching," *Langmuir*, vol. 25, no. 1, pp. 59–63, 2009, doi: 10.1021/la801953z.

[23] L. H. Kang, D. K. Kim, and J. H. Han, "Estimation of dynamic structural displacements using fiber Bragg grating strain sensors," *J. Sound Vib.*, vol. 305, no. 3, pp. 534–542, 2007, doi: 10.1016/j.jsv.2007.04.037.

[24] M. Salari and H. R. Askari, "Theoretical investigation of absorption and sensitivity of nano-plasmonic fiber optic sensors," *Opt. Laser Technol.*, vol. 48, pp. 315–325, 2013, doi: 10.1016/j.optlastec.2012.08.028.

[25] M. A. Mollah, S. M. R. Islam, M. Yousufali, L. F. Abdulrazak, M. B. Hossain, and I. S. Amiri, "Plasmonic temperature sensor using D-shaped photonic crystal fiber," *Results Phys.*, vol. 16, 2020, Art. no. 102966, doi: 10.1016/j.rinp.2020.102966.

[26] H. Zhang et al., "Ultrasensitive Mach-Zehnder interferometric temperature sensor based on liquid-filled D-shaped fiber cavity," *Sensors (Switzerland)*, vol. 18, no. 4, pp. 1–13, 2018, doi: 10.3390/s18041239.

[27] R. Zakaria et al., "Investigation of surface plasmon resonance (SPR) in MoS_2- and WS_2-protected titanium side-polished optical fiber as a humidity sensor," *Micromachines*, vol. 10, no. 7, 2019, Art. no. 465, doi: 10.3390/mi10070465.

[28] F. Mumtaz et al., "Simultaneous measurement of temperature and strain using multi-core fiber with in-line cascaded symmetrical ellipsoidal fiber balls-based Mach-Zehnder interferometer structure," *Prog. Electromagn. Res. C*, vol. 112, pp. 21–34, 2021, doi: 10.2528/PIERC21021002.